Pure Appl. Chem., Vol. 78, No. 5, pp. 905–933, 2006.
doi:10.1351/pac200678050905

Study of single molecules and their assemblies by scanning tunneling microscopy*

J. G. Hou‡ and Kedong Wang

Hefei National Laboratory for Physical Sciences at Microscale, University of Science and Technology of China, Hefei, Anhui, 230026, China

Abstract: The recent rapid advances in nanotechnology, especially those based on molecules, are due in large part to our newly acquired abilities to measure and manipulate individual molecules and their assemblies. Among all the approaches for the study of single molecules, scanning tunneling microscopy (STM) is unique and powerful owing to its ability to accurately probe and control single molecules. High-resolution spatial imaging combined with scanning tunneling spectroscopy (STS) helps scientists investigate and resolve many chemical and physical problems at the molecular level. In this paper, we review our recent studies of single molecules and their assemblies by combining STM experiments and theoretical simulations based on the density functional theory (DFT).

Keywords: scanning tunneling microscopy; scanning tunneling spectroscopy; single molecules; local density of states; self-assembled monolayers; fullerenes.

INTRODUCTION

The scanning tunneling microscope (STM), invented by Binnig and Rohrer, has revolutionized the field of surface science because it has the highest spatial resolution (lateral resolution 0.1 nm, and vertical resolution 0.01 nm) among all electron microscopes [1,2]. In an STM, the direct interaction of wave functions between tip and surface in the subnanometer scale allows it not only to image the surface as a powerful microscope, but also to act as a probe to detect the electronic structure and even to manipulate or create nanostructures. In recent years, chemists have successfully investigated a wide range of problems related to single molecules on surface with the help of STM [3–13]. Those include chemical identification and structural determination of single molecules, electrical conductivity of single molecules, the bond-selective control of single molecular chemical reactions (bonding or bond breaking), rotation and vibration of molecules, surface diffusion, and so on. There is no doubt that STM has extended the ability of scientists in dealing with materials at the atomic and molecular level, and has become a unique and powerful tool for characterizing physical and chemical properties, creating new structures, and exploring new applications for single molecules.

In this paper, we review our recent studies of single molecules [14–20] and their assemblies [14,21–23] by combining STM experiments and theoretical simulations based on the density functional theory (DFT) [24,25].

---

*Paper presented at the 40th IUPAC Congress, Beijing, China, 14–19 August 2005. Other presentations are published in this issue, pp. 889–1090.

‡Corresponding author: E-mail: jghou@ustc.edu.cn

DIRECT VISUALIZATION OF MOLECULAR ORBITALS (MOs)

The principle and operation of an STM is conceptually rather simple [1,2,11]. As shown in Fig. 1, a sharp metal tip is brought close to a sample surface with a vacuum separation about a few ängstroms. A bias voltage (V_S) is applied between tip and sample, which results in electrons tunneling through the vacuum barrier according to quantum theory. The tunneling current varies approximately exponentially with the sample–tip separation width, thus this tunneling current intensity can be used as a parameter to adjust the sample–tip separation width by feedback loop. When the tip scans over the sample surface, keeping the tunneling current intensity invariable, a 2D tip height map can be obtained. If the feedback loop is closed, a current map is obtained as constant height image.

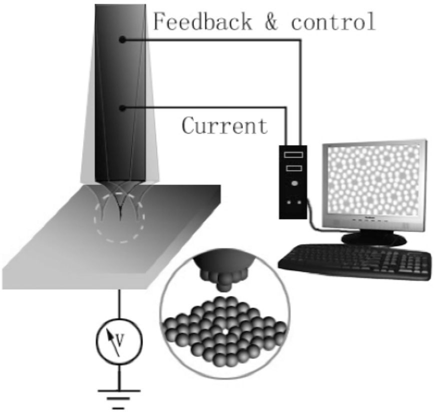

Fig. 1 Diagram of an STM.

Complexities of STM imaging [11]

In principle, STM imaging is very appropriate for visualizing MOs directly in real space owing to its very high lateral resolution. In practice, there are still problems and challenges for both the experimental and theoretical application of STM to molecules because of various intrinsic and extrinsic factors that can influence the STM imaging process and reinforce the difficulties in the interpretation of the intramolecular pattern and its relation to the real molecular structure.

First, the image contrast, or the internal pattern of a nanostructure, is usually not directly related to the atomic structure and topography of sample because the tunneling current is mainly dependent on the low density of the occupied states (LDOS) distribution near the Fermi level (E_F) [2]. For example, cobalt phthalocyanine (CoPc) and copper phthalocyanine (CuPc) both have a metal atom at the center of the crisscross molecules (Fig. 2). In a negative-bias STM image, a bright spot was observed at the center of the CoPc molecule (Fig. 2a) corresponding to the metal atom. In the CuPc image (Fig. 2b), however, the center is actually darker than the lobes [20], because of the LDOS near E_F at the center of CuPc.

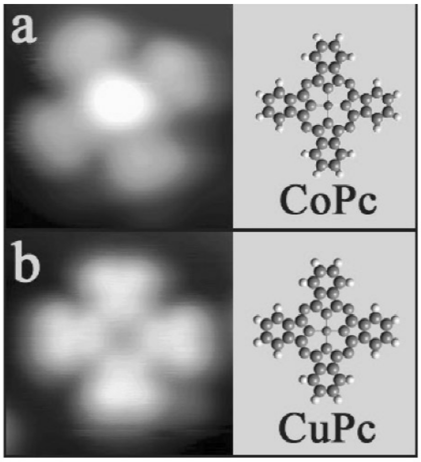

Fig. 2 Negative-bias (–0.7 V) STM images of CoPc (a) and CuPc (b) molecules adsorbed on Au(111) surface, respectively.

Second, the image contrast also depends on the bias polarity. When the V_S of the sample relative to the STM tip is positive, electrons tunnel from the tip to the unoccupied states of the sample (Fig. 3a), and when V_S is negative, electrons tunnel from the occupied states of the sample to the tip (Fig. 3b). So different V_S polarity determines the different states of the sample that contribute to the STM image. For example, we can see a blurred cage in the positive-bias STM image of Dy@C_{82} molecule adsorbed on Au surface, while the negative-bias image shows curved stripes (Fig. 3).

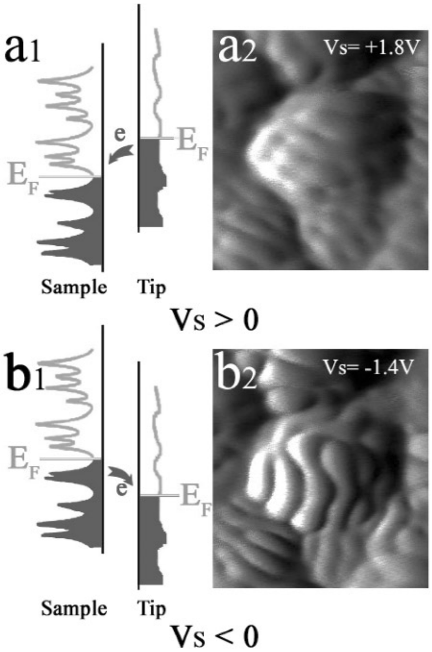

Fig. 3 Schematic figures for the origin of the V_S dependence of STM image [(a1) and (b1)]: different V_S determines that different electronic states of sample contribute to STM image. (a2) and (b2) show images of one Dy@C_{82} molecule on Au(111) surface under different V_S.

Third, the structure of the STM tip is crucial and determines the pattern contrast as well as the qualities of the obtained images [26]. Figure 4 shows two sets of STM images of C_{60} molecules, which were simulated with the same parameters of measurement but using different tips: one is a metal tip, the other is a tip adsorbed with another C_{60}. Obviously, the differences between intramolecular patterns of the upper and lower images result from different tip terminal structures [11].

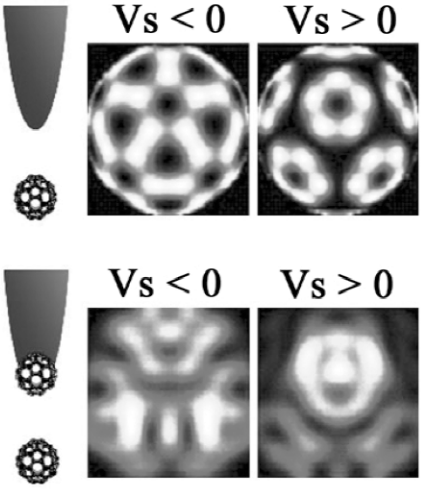

Fig. 4 Simulated STM images of C_{60} by using a metal tip (upper) and a tip adsorbed with another C_{60} (lower).

Fourth, in order to get high-quality tunneling current images, molecules must be put on electrical conducting surfaces such as a metal or a semiconductor substrate. When the molecules adsorbed on such surfaces, the molecule–substrate interaction (i.e., bonding or charge transfer) may change the electronic structure of the adsorbed molecules, especially near E_F, and thus the STM images of same molecules may be different when they adsorb on different substrates. Figure 5 shows STM images of C_{60} adsorbed on two different surfaces—one is on a Si(111)-7 × 7 surface [15], and the owing to the similar molecular orientations, the fine structures are significantly different. When C_{60} is adsorbed on a Si(111)-7 × 7 surface, the C_{60} is bound with the Si substrate by covalent bonds with a small amount of ionic bonds mixed in [15]. When C_{60} is adsorbed on a Cu(111) surface, however, the threefold symmetric intramolecular features were shown to be caused by the charge transfer from Cu to C_{60} [27].

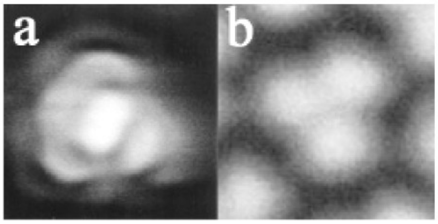

Fig. 5 Positive-V_S STM images of C_{60} molecules adsorbed on Si(111)-7 × 7 (a) and Cu(111) (b) surfaces. Both images exhibit the threefold symmetry but different fine structures. Figure (b) is reprinted from ref. 27 [27].

Native structure of C_{60} revealed by STM [14]

Though the interior pattern of STM images of single molecules depends on different factors as discussed above, it is still fundamentally interesting to directly visualize MOs with STM. Owing to its spherical cage structure, the C_{60} molecule has attracted considerable interest since its discovery [28,29], and many attempts have been made to unveil its internal cage structure with STM [27,30–32]. However, only a few authors reported STM images of C_{60} that reveal some intramolecular features but could not be directly correlated with the cage structures [27,30–33]. For example, STM images with four slightly curved bright stripes were typically obtained for C_{60} adsorbed on the Si(111) and Si(100) surfaces [30,31,33], regardless of their different surface atom arrangements and binding configurations. Because of the strong C_{60}–substrate interactions, these experiments have left the challenge of directly visualizing the native structure of C_{60} largely unanswered.

In order to directly image the C_{60} molecular native structure, the molecule–substrate interaction must be blocked. In our experiments [14], alkylthiol self-assembled monolayer (SAM) was introduced between the C_{60} molecules and the gold substrate. The thiol SAM was used because of its inert chemical property. The alkylthiol SAM substrate was prepared by solution method [22,23] and transferred into the ultra-high-vacuum (UHV) STM chamber where a submonolayer of C_{60} was then thermally evaporated onto it. The STM images show that at room temperature, C_{60} displays a smooth hemispherical protrusion, suggesting that the C_{60} molecules are rotating freely at this temperature.

When the sample is cooled down to 5 K, C_{60} molecules in the STM image start to reveal an identical internal fine structure (Fig. 6a) that closely matches the well-known cage structure (Fig. 6b). Figure 6c shows a simulated STM image of a C_{60} structure obtained by integrating the electron density of states (DOS) on a C_{60} from the Fermi level to the V_S, where the DOS of C_{60} was calculated using the discrete variational-local density approximation (LDA) method (DVM) [34,35]. The C_{60} orientation is tuned for the best agreement between the simulation and the experiment. One can see that the simulated image matches the experimental one very well.

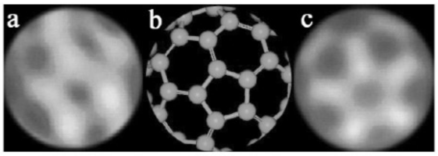

Fig. 6 The native cage structure of C_{60} molecules seen using an STM. (a) STM image of a C_{60} molecule taken at 5 K with –2.0 V sample bias. Detailed internal features of the C_{60} molecule are evident that closely resemble the C_{60} cage structure (b) and match the theoretical simulation shown in (c).

Identifications of molecular orientations on surfaces

Structured molecules differ significantly from the simple elemental adsorbates because of their 3D character on the atomic scale. A unique fundamental property of this type of adsorbates is the molecular orientation with respect to the host substrate. When an isolated molecule ceases its rotational motion on a surface, it may, in general, adopt a number of binding configurations and hence a multitude of orientations. This new property could serve as the basis for designing new catalysts with functionalized cage molecules or for fabricating thin films of desirable orientational orders. Thus, understanding how molecules orient themselves on a substrate is obviously a worthy but challenging task both theoretically and experimentally. In the following sections, we will show how to determine the orientation of the molecules on surfaces with the help of high-resolution STM images and theoretical simulations.

2D C_{60} films on SAM [14,21]

2D systems possess a unique topological ordering that is not found in either 3- or 1D systems [36]. Using high-resolution STM, we show here that a C_{60} array on an alkylthiol SAM forms an ideal 2D system, which has another novel topological order originating from the orientational degrees of freedom [14,21].

STM images show that C_{60} molecules on SAM form close-packed hexagonal arrays, with a nearest-neighbor distance of 10 Å. As the samples cooling down to 5 K, all C_{60} ceased its rotational motion and formed orientationally ordered domains (Fig. 7) unlike the orientation-related glassy phase in bulk C_{60}. The remarkable conformity between the simulated image of C_{60} on SAM and the experimental one introduced in the last section allowed us to confidently identify the C_{60} domain with certain molecular orientations as shown in Fig. 7 (stick model). These observations, together with the fact that the C_{60} molecules are not in an epitaxial (or commensurate) arrangement with respect to the SAM, are indicative of a very weak interaction between the C_{60} and the alkylthiol.

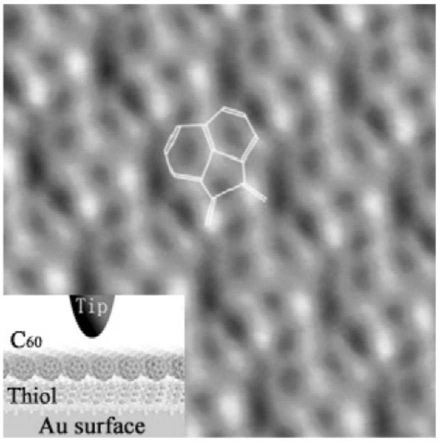

Fig. 7 An orientational-ordered 2D C_{60} domain (35 × 35 Å) taken with –2.0 V at 5 K. The stick model shows the orientation of C_{60} molecules. Inset shows the diagram of the experiment.

Although most of the C_{60} arrays feature a single orientation, we have also observed a single array consisting of domains of two different orientations (Fig. 8), in which the boundary separates two distinguishable domains by their internal features. Comparison with our simulation results enabled us to identify these two orientations as those shown in Fig. 8 inset. Apart from the two different molecular orientations, there is no positional defect at the domain boundary, and the entire C_{60} array maintains the perfect translation symmetry for the centers of the C_{60}.

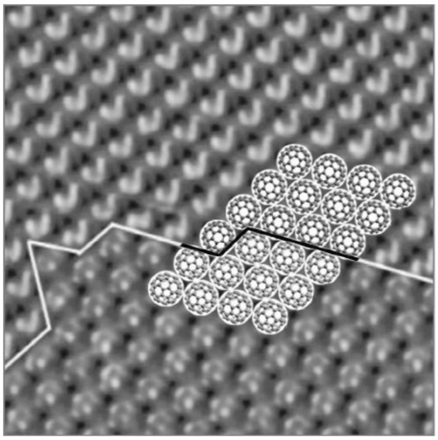

Fig. 8 Orientational-ordered 2D C_{60} domains and the domain boundaries.

Experimental results encouraged us to employ some theoretical works to understand these unique orientational orders and domain structures [21]. Using total energy optimization with a phenomenological potential, we find the ground state is a close-packed hexagonal lattice in which all the molecules have the same orientation. Several local minima of the potential energy surface are found to be associated with other 1 × 1 lattices as well as 2 × 2 lattices. The energies for the identical orientational orders such as the ones observed experimentally are, indeed, among several local minima, if not the global minimum. Furthermore, the energies of the orientational domain boundaries of the 1 × 1 lattices are also computed, and two kinds of which yield negative values (Fig. 9).

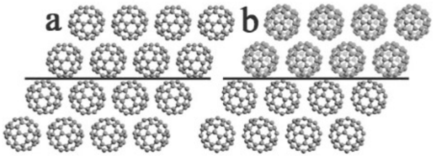

Fig. 9 Theoretical domain structures with negative boundary energies.

Through the model computation as well as the STM experiment, we have shown that orientational ordering in a 2D C_{60} is drastically different from that in a C_{60} solid. In particular, the reduced dimensionality allows the molecules a greater degree of freedom in adjusting their mutual orientations. Although the interface orientations have lower symmetry than those in the 3D case, they better minimize the system energy and the domain boundary energies and lead to a deliberate uniorientational molecular order for a 2D C_{60} and a new topological order for the orientational domains. These findings will have implications in other molecular lattices as well as in lattices made of more complex building blocks such as clusters.

C_{60} *on Si(111)-7 × 7 [15]*

We have shown that the orientations of the C_{60} molecule on SAMs can be simply identified by comparing the STM image with the native cage structure of C_{60} [14]. However, when C_{60} adsorbed on a metal or semiconductor surface, the intramolecular features in STM images could not be directly correlated with the cage structures owing to the C_{60}–substrate interactions. Theoretical calculations are necessary to help identify the orientations of the C_{60} in such systems.

Here, we show that the molecular orientation of the adsorbed C_{60} with respect to a Si(111)-7 × 7 surface can be determined unambiguously by combining low-temperature STM experiments with LDA calculations [15].

Si(111)-7 × 7 substrate was prepared by a standard procedure [15]. Sub-monolayer C_{60} molecules were deposited onto Si(111)-7 × 7 surface via sublimation, and STM experiments were carried out at a base pressure below 3×10^{-11} Torr with an electrochemically etched W tip at 78 K. Figure 10a is a high-resolution image showing the internal patterns of four C_{60} molecules (3D display). Four possible adsorption sites (Fig. 10b) have been observed.

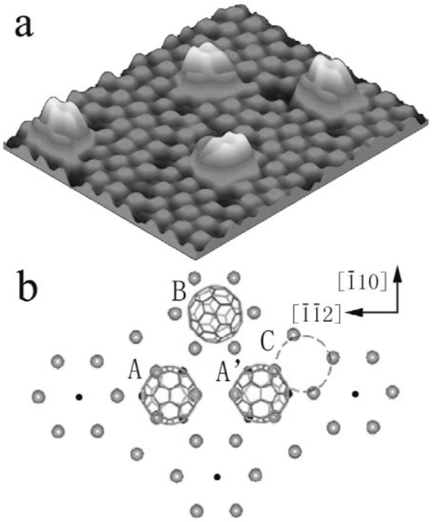

Fig. 10 (a) STM image of four C_{60} molecules on Si(111)-7 × 7 surface. (b) Four possible adsorption sites.

The internal pattern of the C_{60} depends strongly on the V_S and the tip–sample distance. At site A, the feature of the large positive-bias image is one bright pentagon ring plus two curved strokes (Fig. 11a3). Similar reproducible results were also obtained for C_{60} molecules on site A_0. At adsorption site B, the internal pattern of C_{60} at positive sample bias is a bright pentagon ring plus three curved strokes to its right (Fig. 11b3). The reproducible high-resolution STM images with clear intramolecular features of C_{60} raise the possibility of identifying the molecular orientations on Si(111)-7 × 7 surface.

STM images were simulated adopting the Tersoff–Hamann method [37]. For a given adsorption site, we considered five different C_{60} high-symmetry rotational orientations, i.e., a hexagon, a 6–6 bond, a 5–6 bond, a pentagon, and an edge atom facing toward the Si substrate, respectively. The electronic structures of $C_{60}Si_{57}H_{42}$ (for C_{60} adsorbed on site A), and $C_{60}Si_{67}H_{45}$ (B site) cluster were calculated using the DVM [34,35]. The simulated STM images show that the positive-bias images depend strongly on the orientation of C_{60} on the substrate and less on the adsorption sites. Comparing our simulations with the experiment, we find that the experimental image of C_{60} on the A site (Fig. 11a3) best matches Fig. 11a4 (a bright pentagon ring plus two bright curved strokes to its left); while the image of C_{60} on the B site (Fig. 11b3) best matches Fig. 11b4 (one bright pentagon ring plus three bright curved strokes to its right). We thus conclude that the C_{60} is adsorbed on site B with one of the edge atoms facing toward the Si substrate, and has one of the 5–6 bonds facing toward the surface on site A (or A_0).

Our calculation also shows that C_{60} is bound with Si substrate by covalent bonds with a small amount of ionic bonds mixed in. Because of this strong interaction, the electronic structure of C_{60} molecule is modulated, and a stripe-like internal structure appears in the negative-bias image.

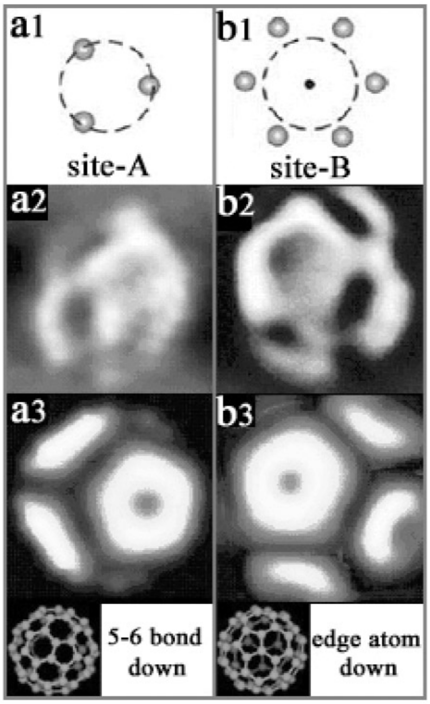

Fig. 11 STM images [(a2) and (b2)] and the theoretical simulations [(a3) and (b3)] of C_{60} on different adsorption sites [(a1) and (b1)] of Si(111)-7 × 7.

C_{120} molecules on Au(111) surface

C_{60} can be polymerized by many methods and the dimer is the simplest product [38–42]. Theoretical works [43,44] predicted that the most energetically favorable bonding between the two C_{60} molecules is accomplished by breaking the hexagon–hexagon π-bonds associated with the two polar atoms on each ball and then forming σ-bonds between the two balls ([2+2] cycloaddition). In 1997, G. W. Wang et al. found [45] that the solid-state mechanochemical reaction of C_{60} with potassium salts such as KCN under "high-speed vibration milling" conditions can mass produce the dimer of C_{60}. Their ^{13}C NMR, X-ray crystallography, and UV–vis spectrum results proved the [2+2] cycloaddition configuration (Fig. 12). Previous STM works [46,47] found that the self-assembled adlayer of C_{120} formed $2\sqrt{3} \times 4\sqrt{3}$ R30°, $2\sqrt{3} \times 5\sqrt{3}$ R30°, and 7 × 7 lattices on the Au(111)-1 × 1 surface.

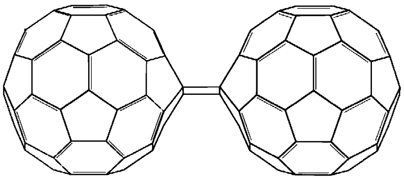

Fig. 12 A stick model of C_{120} molecule.

In our experiments, the orientations of the adsorbed C_{120} molecules on a Au(111) surface can be clearly determined by comparing high-resolution STM images with theoretical simulations.

Owing to the ready thermal cleavage [45], we first purified the C_{120} sample powder by immersing it in toluene four times to remove the production of thermal cleavage, i.e., the C_{60} molecules. Then the remaining powder was dissolved and diluted in *o*-dichlorobenzene. A proper sheet of Au film was dipped into the C_{120} solution for 10 s, and then the sample was transferred into the UHV system immediately after it dried in pure (>99.9 %) nitrogen atmosphere. The STM works were performed at 78 K.

The STM image (Fig. 13) shows that all the C_{120} molecules lay on the Au surface and each one was revealed as a dumbbell. The existence of intramolecular features in the STM image implies that the C_{120} ceased its diffusion and rotation at 78 K on the Au(111) surface.

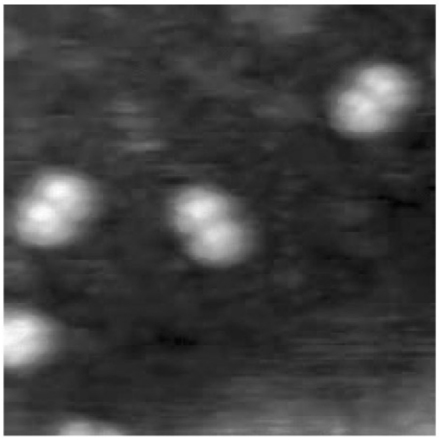

Fig. 13 A 15 × 15 nm STM image of C_{120}/Au sample. $V_S = 1.8$ V, $I = 0.3$ nA, and $T = 78$ K.

It is enlightening that when we focused on the “dumbbells”, four different adsorption orientations were found. Figure 14a*i* (*i* = 1–4) shows the four orientationally different C_{120} molecules on Au surface observed by STM. The simulated images (Fig. 14b*i*, *i* = 1–4) was obtained by integrating the electron DOS on a C_{120} from the Fermi level to the V_S according to the molecular orientations as shown in Fig. 14c*i* (*i* = 1–4), which match the experimental ones very well. Furthermore, the molecular images shown in Fig. 14 all are mirror symmetrical, fully consistent with the D_{2h} symmetry of the C_{120} molecules.

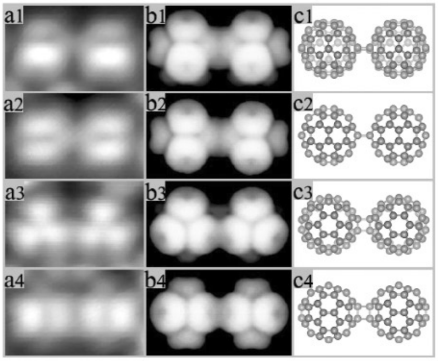

Fig. 14 (a*i*) (*i* = 1–4) show the STM images of orientationally different C_{120} molecules ($V_S = 2.0$ V, $I = 0.3$ nA), (b*i*) (*i* = 1–4) show the simulated images with the molecular orientations as shown in (c*i*) (*i* = 1–4).

Thiol SAMs on Au(111) surface [22,23]

The SAMs have shown advanced applications in chemical sensing, biosensing, biomimetics, and molecular electronics, and significantly contribute to the general understanding of the fundamental physics and chemistry of complex surfaces and interfaces [48,49]. Different diffraction techniques such as low-energy electron diffraction (LEED) and reflection high-energy electron diffraction (RHEED), spectroscopy-based techniques like X-ray photoelectron spectroscopy (XPS), infrared (IR), etc., and microscopy techniques such as STM and atomic force microscopy (AFM) have been used for the characterization of the molecule-scale structure of alkanethiol SAMs on Au(111) [49,50]. Although the basic structure of alkanethiol SAMs on Au(111) has been ascertained with quantitative precision [51–57], it is still a challenge to fully understand the electronic properties of the insulating alkanethiol SAMs on the Au(111) surface, and to interpret the internal patterns in STM images due to long insulating alkyl chain and almost standing molecular configuration.

In our studies, heptanethiol SAMs were prepared by solution method. STM images show c(4 × 2) superlattices of a $(\sqrt{3} \times \sqrt{3})$ R30° hexagonal lattice (Fig. 15). When V_S is in the range from 0.5 to 1.5 V, only bright intensity modulation of the spots in the hexagonal lattice can be resolved with one bright spot and three gray spots in a primitive unit cell. When V_S is larger than 1.5 V, all the gray spots turn to striped shapes, and the bright spots mainly keep their original shapes. When V_S is changed to negative, the gray spots observed at low positive V_S turn to dumbbell shapes, and the bright spots are almost unchanged. No obvious variation is observed when V_S varies from –0.5 to –2.5 V.

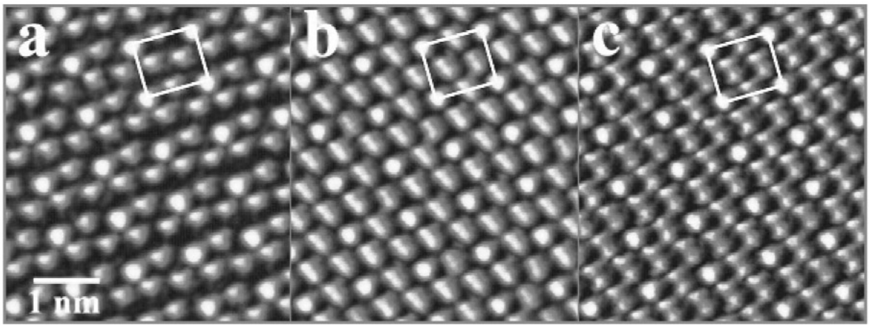

Fig. 15 STM images of heptanethiol SAM with c(4 × 2) superlattice: (a) $V_S = 0.5$ V, (b) $V_S = 2.0$ V, (c) $V_S = -1.5$ V.

We simulated STM images with the Tersoff–Hamann method [37], and also calculated the electronic structure calculations by DFT [24,25]. In our case, a cluster model including only one molecule and 22 Au atoms (three layers) was adopted for the electronic structure calculation and subsequently the STM image simulation because of the van der Waals interaction between the alkanethiol molecules.

Sp3-hybridization, and sp-hybridization (Fig. 16c) energetically favorable orientational configurations [58] were investigated theoretically. For the sp mode, the simulated molecular pattern is always a bright spot at V_S ranged from –2.5 to 2.5 V. For sp3 mode, when V_S is negative the intramolecular pattern is always a dumbbell shape. The experimental and simulated images at $V_S = -1.5$ V for a primitive unit cell of heptanethiol SAM are both shown in Fig. 16, with three sp3 modes and one sp mode, which agrees well with the theoretically optimized packing structure [59].

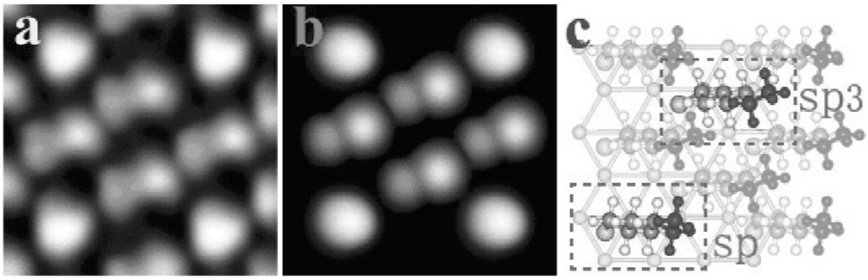

Fig. 16 (a) and (b) are the experimental and simulated STM image of a primitive unit cell for c(4 × 2) superlattice of heptanethiol SAM ($V_S = -1.5$ V), respectively. (c) is schematic diagram of the SAM. One unit cell contains three sp3 mode and one sp mode molecules.

The electronic structure calculations showed that there is a big gap between the highest occupied molecular orbital (HOMO) and the lowest unoccupied molecular orbital (LUMO) of the heptanethiol molecule. Its HOMO and LUMO are mainly dominated by S component, and the percentage of S atomic orbitals is more than that of the terminal CH_3 group orbitals by four orders of magnitude. During the adsorption process of alkanethiol molecule onto the Au(111) surface, the S–H bond is broken and the S atom is bonded to the Au(111) surface [60], many new orbitals appear in the original HOMO-LUMO and (HOMO-1)-HOMO gaps of heptanethiol molecule. Most of these orbitals are from plain Au bulk states. However, in some new orbitals, the percentages of S and alkyl part states are obviously more than that in other orbitals. Such orbitals result from the intermixing of MOs and substrate states induced by the strong interaction between alkanethiol molecule and Au substrate. Electrons' transiting by these MOs enables STM imaging for alkanethiol SAMs.

Calculations also validated that the information detected by the STM tip indeed reflected the terminal part of the hydrocarbon chain of the alkanethiol molecule. Alkanethiol molecule is chemisorbed on the Au(111) surface with ~30° tilt angle from the surface normal, so the terminal part of the hydrocarbon chain of alkanethiol molecule is closer to the STM tip than the Au-bound S atom with ~8 Å height difference. Commonly, the LDOS in the vacuum beyond the materials surface decays quickly with increasing distance from surface. Therefore, when the electronic effect and the topographic effect are combined for consideration, the dominance of Au-bound sulfur orbitals in DOS is reversed, and in the region probed by the STM tip, the electronic wave function is localized near the terminal part of the hydrocarbon chain.

SCANNING TUNNELING SPECTROSCOPY (STS) OF SINGLE MOLECULES

In order to understand the electronic transport properties of single molecules, and thus to explore the possibility of device application, it is very important for us to get current–voltage (I–V) spectrum of molecules between two electrodes. A natural method is to fabricate nano-electrodes with a separation of a few nanometers using lithographic techniques and put molecules between them. In recent years, tunneling gaps of a few nanometers have been fabricated with novel methods based on lithographic techniques [61,62]. But it is still not easy to measure the electrical properties of single molecules by this method owing to the low yields and reproducibility in making the nano-electrodes, and the difficulty in putting the molecule just right between the two electrodes.

STM provides an easier way to form a two-electrode measurement system for molecules: the STM tip and a supporting substrate serve as the electrodes; the electronic transport property can be measured through STS. Since the tunneling current I reflects an integral of LDOS, the normalized $d\ln I/d\ln V = (dI/dV)/(I/V)$ is approximately proportional to the LDOS [2,37]. Furthermore, d^2I/dV^2 that contains the inelastic electron tunneling signal was successfully used to detect molecular vibrational information [3,8].

On the other hand, the STS measurement and data analysis are still not simple works because of the existence of interactions between the molecule and the substrate or even the tip. Generally, there are three configurations in the STS measurement of molecules (Fig. 17). When the molecule is chemically adsorbed onto a metal or semiconductor surface and the tip is also contacted with the molecule, a direct-connect mode was realized (Fig. 17a). If there is a vacuum separation between the tip and the molecule, a single-barrier tunneling junction (SBTJ) geometry is formed (Fig. 17b). In these two modes, the interactions between the molecule and the substrate or tip are important and dramatically influence the *I–V* characters. A double-barrier tunneling junction (DBTJ) system was formed (Fig. 17c) only when the molecule–substrate interaction was also blocked. The original properties of the molecules as well as a single-electron tunneling (SET) effect are expected be observed in such system. As examples, the transport properties of a C_{60} molecule in the above three junctions are discussed below.

C_{60} has the spherical structure, which results in a close-shell electronic structure consisting of highly degenerate η- and σ-derived molecular electronic states including η-derived fivefold degenerate HOMO and a triply degenerate LUMO [63]. The energy gap between the HOMO and LUMO is determined to be about 1.7 eV by using the ab initio calculation [64] and 1.8 eV experimentally [65]. The unique electronic and structural properties of C_{60} allow us to foresee a promising future for this type of molecule as building blocks in future single-molecular devices.

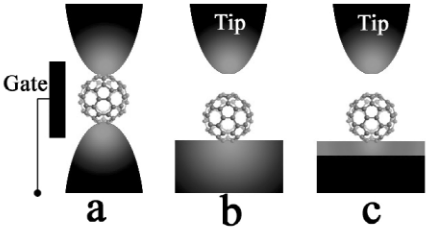

Fig. 17 Diagrams of different method for the measurement of molecular electronic transport properties: directly connected with two electrodes (a), in an SBTJ (b) and in a DBTJ geometry (c).

Jeremy Taylor et al. proposed a model transistor [66] in which a C_{60} molecule was bonded by two atomic-scale Al metallic electrodes that extended to reservoirs far away. An additional gate voltage was also applied to a metallic gate capacitively coupled to the molecule (Fig. 17a). An approach that combines nonequilibrium Green's function theory with pseudopotential real-space DFT simulation techniques was developed to investigate this model transistor. The theoretical results suggested that charge-transfer doping induced a substantial conductance in a well-contacted molecular C_{60} device. Three transferred electrons half filled the LUMO state and contributed three conduction channels at equilibrium, producing metallic *I–V* characteristics. A field effect provided by a gate potential can switch off the current by inhibiting charge transfer.

When STM is used to investigate the C_{60} molecule adsorbed on different conducting surfaces, an SBTJ system is formed. From the STS investigation, it was found that the HOMO–LUMO gaps of C_{60} adsorbed at sites A, B, and C of Si(111)-7 × 7 surface (see the section "Identifications of molecular orientations on surfaces") are 1.4, 0.8, and 1.3 eV (Fig. 18), respectively, much smaller than that of free C_{60} molecules [16]. It was confirmed that the mixing states of the C_{60} orbitals with the LDOS of Si(111)-7 × 7 are site-dependent owing to the strong interaction between the C_{60} and the dangle bonds of the surface and the different surface structures at different sites. These interactions also influenced the STM images [15].

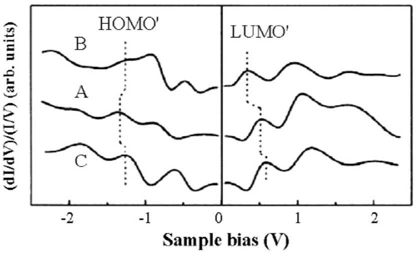

Fig. 18 A, B, and C are the STS results corresponding to C_{60} adsorbed at sites A, B, C on Si(111)7 × 7 surface, respectively.

Orbital-related fine structures in the *I–V* curve of C_{60} in a DBTJ [10]

When C_{60} molecules adsorbed on top of well-characterized alkanethiol SAMs deposited on an Au(111) surface, a DBTJ configuration was realized in which a C_{60} molecule is coupled via two tunnel junctions to the metal substrate and the tip of the STM (Fig. 17c). As expected, SET effect was observed in this system because the charge energy of this nanojunction is much larger than the thermal fluctuation energy. In Fig. 19 inset, typical measured *I–V* curves of a single C_{60} molecule in DBTJ at 5 K were given, and the fine structure of the spectrum can be quantitatively understand by the orthodox theory for the SET effect of quantum dots in DBTJ together with the electronic structure of C_{60}.

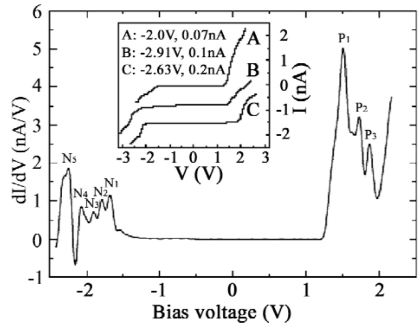

Fig. 19 A numerical differential STS spectrum of a C_{60} in a DBTJ (V_S = 2.0 V; I = 0.2 nA). Inset shows three *I–V* curves of C_{60} in DBTJ.

According to the orthodox theory [67,68], to add (+) [remove (–)] an electron to (from) the quantum dot through one junction, work has to be done against the electric field of excess electrons (ne) which already reside on the quantum dot as

$$E_C^{\pm}(n) = e^2\left(\frac{1}{2} \pm n\right) / \left(C_1 + C_2\right)$$

in which E_C is the charging energy, C_1 and C_2 are the capacitances of the two junctions, respectively. This charging energy induces the zero current gap—Coulomb blockade (CB) and Coulomb staircase in the *I–V* curve.

To simplify discussions below, we assume that $C_1 < C_2$ in our system. This means that the first tunneling electron will always span the first junction. According to the orthodox theory, the CB thresholds of the negative and positive voltages are deduced from the law of partial voltage:

$$V_+ = V_- = \frac{C_1 + C_2}{C_2 e} E_C(0)$$

For a single molecule, however, there is a discrete energy level structure, so additional work due to the discrete level effect should be taken into account. For a molecule such as C_{60}, with a fully occupied HOMO, its E_F locates between the HOMO and LUMO when the molecule is neutral. When the first tunneling electron spans the first junction, the LUMO (HOMO) will be occupied (unoccupied). Therefore, the accessional energies required by the discrete level effect for the addition (reduction) of one electron to (from) the molecule through the first junction equal to energy differences between Fermi level and LUMO or HOMO. After getting or losing one electron, the molecule will be ionized with a partially occupied level. The E_F will shift up/down to coincide with this partially occupied level. Therefore, there is no accessional energy required by the discrete level effect for the tunneling of the second junction. Although the precise position of the E_F shows some randomness in the measurements, it locates near the middle of the HOMO and LUMO generally when the molecule is neutral. If we assume that the position of the Fermi level lies in the middle of HOMO and LUMO, the CB thresholds of the negative and positive voltages are:

$$V_+ = V_- = \frac{C_1 + C_2}{C_2 e}\left[E_C(0) + E_g/2\right]$$

Thereby, the CB of C_{60} molecule in a DBTJ is nearly symmetric because of the fully occupied HOMO and LUMO molecular states.

According to the previous discussions, the CB should be

$$\Delta V_C = V_+ + V_- = \frac{C_1 + C_2}{C_2 e}\left[2E_C(0) + E_g\right]$$

by assuming $C_2 > C_1$. As the setting-point voltage $V_S = 2.0$ V and current $I = 0.2$ nA and considering the tip as a semisphere, the capacitance C_1 of junction 1 between the STM tip and the C_{60} molecule is estimated to be 0.02 aF. Using the thickness of the SAM at about 9.68 Å [69], and the dielectric constant for SAM on Au(111) at about 2.6 [70], we have calculated the capacitance C_2 of junction 2 between the C_{60} molecule and Au substrate to be about 0.15 aF [71]. From the orthodox theory, the E_C is calculated to be about 0.47 eV, and ΔV_C is calculated to be about 2.8 V (Fig. 20), which agrees with the experimental data perfectly (Fig. 19). When the STM tip approaches the molecule, the capacitance of the tip-molecule C_1 will increase. From the orthodox theory, ΔV_C will increase to 3.1 eV when C_1 increases to 0.045 aF. In our experiment, ΔV_C is measured to reach 3.0 eV when I is set at 1.5 nA.

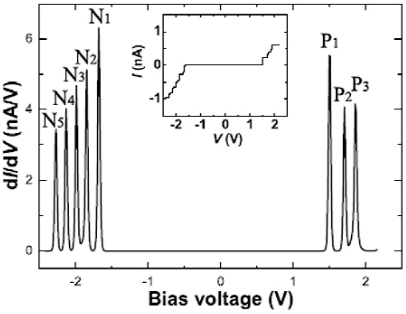

Fig. 20 Calculated *dI/dV* spectra of C_{60} in DBTJ.

Despite the CB, we notice that there are fine peaks in the numerical calculated *dI*/*dV* curves, which correspond to the fine steps in the *I*–*V* spectrum. According to the experiments, the fine peaks are always fivefold (Fig. 19, N*i*, *i* = 1–5) or triplex (Fig. 19, P*i*, *i* = 1–3). We consider that these fine peaks reflect the split of C_{60} molecular fivefold degenerate HOMO and triply degenerate LUMO. The SET effect is responsible for the splitting of the MOs. Theoretical calculations reproduced the fine peaks (Fig. 20).

Single-molecular rectifier using an azafullerene $C_{59}N$ molecule [18]

As we use the $C_{59}N$ molecule to replace the C_{60} in a DBTJ, we will show that the half-occupied MO of the $C_{59}N$ molecule and the asymmetric shift of the molecular Fermi level when the molecule is charged result in a new kind of molecular rectifying effect. The synthesis method of $C_{59}N$ is reviewed in ref. [72]. The STM experiments are similar to C_{60}.

Figure 21 shows a typical set of tunneling *I*–*V* curves for individual $C_{59}N$ molecules measured at various setting parameters by positioning an STM Pt-Ir tip above a $C_{59}N$. Different from the *I*–*V* curves of C_{60} molecules shown previously, pronounced asymmetry of CB is observed, and this rectifying effect is repeatable for all measurements we made. We find that although the detailed feature of each curve is varied slightly due to the different setting parameters, the positive onset sample V_S (V+) is always about 0.5–0.7 V, while the negative onset sample V_S (V–) is about 1.6–1.8 V.

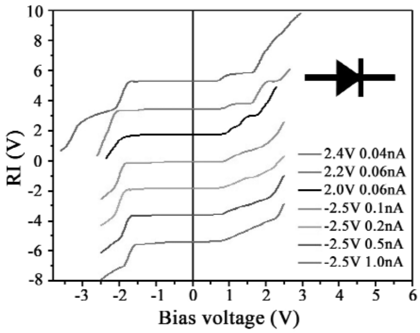

Fig. 21 A set of *I*–*V* curves for individual $C_{59}N$ molecules measured at 5 K with various setting parameters. For clarity, we use *RI*, instead of *I*, as the vertical axis, and shift the curves vertically, where *R* is the asymptotic resistance and estimated from the slope of the *I*–*V* curve.

Figure 22a shows the energy level diagram of a free $C_{59}N$ molecule, which is calculated using DFT with LDA implemented with the Dmol^3 package [73]. The HOMO orbital of $C_{59}N$ is half occupied with one electron. The Fermi level coincides with the half-occupied HOMO when the molecule is neutral. Accordingly, there is no accessional energy required by the discrete level effect for the tunneling of the first junction. Then, by assuming $C_1 < C_2$, the CB thresholds of the first junction are deduced to be

$$V_+^1 = V_-^1 = \frac{e}{2C_2}$$

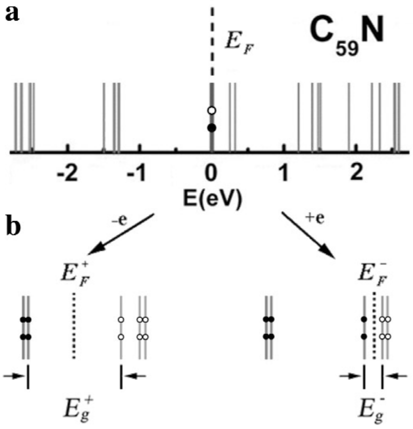

Fig. 22 (a) The energy level structures of $C_{59}N$. (b) A schematic diagram for the changes of the Fermi level of a $C_{59}N$ molecule in the DBTJ.

After receiving or losing one electron, the molecule will have fully occupied HOMO and unoccupied LUMO (Fig. 22b). For the tunneling of the second junction, since the new E_F is lying between the new fully occupied HOMO and unoccupied LUMO, therefore, the accessional energy is required by the discrete level effect. Assuming that the new energy gaps after receiving or losing one electron are E_g^- and E_g^+, respectively. Then the thresholds for electron tunneling through the second junction should be:

$$V_{\pm}^{2} = \left(1 + \frac{C_2}{C_1}\right)\frac{E_g^{\pm}}{2e} - \frac{e}{2C_1}$$

V_+ and V_- are decided by $V_+ = Max(V_+^1, V_+^2), V_- = Max(V_-^1, V_-^2)$.

From the formula above, one can see that if E_g^- and E_g^+ are significantly different, V_+ and V_- will be remarkably different generally. This is the main reason for the novel rectifying effect.

We can quantitatively calculate the CB thresholds using the formula above. Similar to the discussions of the C_{60}-DBTJ system, we evaluate the capacitance of junction 1 between the STM tip and $C_{59}N$ molecule (C_1) to be 0.012– 0.015 aF according to the small tunneling current in experiments and C_2 to be about 0.15 aF. Due to theoretical calculations, the E_g^- and E_g^+ of $C_{59}N$ are 0.25 and 1.29 eV, respectively. Then, it can be obtained easily that: $V_+ = 0.53$ V; $V_- = 1.76 \sim 2.04$ V. These CB thresholds agree with the experimental ones. So we concluded that the half-occupied HOMO and the significant difference between E_g^- and E_g^+ together with the SET effect are responsible for the novel rectifying effect.

From these results, we can see that fullerenes serve as ideal quantum dots in mesoscopic junctions, due to their small size and well-known electronic structure. The good agreement with the orthodox shows the interplay between the charge effect and the resonant tunneling of discrete energy levels could be controlled to get required tunneling properties. These investigations are not only of the fundamental physical interest, but also are effects that could set the limit of future devices operating on the transfer of single electrons.

SPATIAL AND ENERGETIC MAPPING OF SINGLE MOLECULES [17]

Endohedral metallofullerenes have been a subject of intensive investigation in recent years [74]. The location of metal atoms inside the fullerene cage and the metal-cage interaction are two central issues. Most of the investigations require macroscopic quantities of metallofullerenes and give either ensemble-averaged or spatially averaged results [75–79]. It has been a challenging task to characterize the local properties of isolated metallofullerene molecules.

Since a normal STM topological image reflects the integrated LDOS of the sample surface from E_F to $E_F + eV_S$, and the STS only provide the LDOS information of the tip pointed area, the spatial distribution of LDOS could not be fully characterized by these two methods. One solution is to map the *dI/dV* signal at every point on the topography image. Since the value of *dI/dV* is approximately proportional to the intensity of LDOS at the energy of $E_F + eV_S$ (Fig. 23), the *dI/dV* mapping method can spatially map the energy-resolved LDOS of a molecule [37,80]. Experimentally, an $\Delta I/\Delta V$ data could be obtained through lock-in detection of the alternating tunneling current driven by modulating the sample bias with the feedback loop open. As the window ΔV is small enough, the $\Delta I/\Delta V$ is approximate to *dI/dV* mathematically. Next, we will show that a *dI/dV* map method is very useful in identification of special molecular structures like endohedral metallofullerenes.

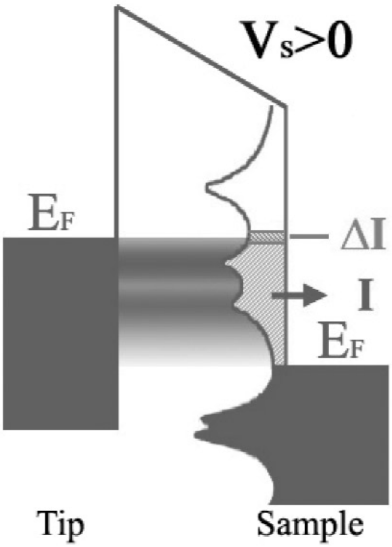

Fig. 23 Differences between tunneling current and the ΔI window. The integral of LDOS from Fermi level to $E_F + eV_S$ contributes to the tunneling current, while the ΔI window reflects the intensity of LDOS around $E_F + eV_S$.

The sample was prepared by depositing a submonolayer of Dy@C_{82} isomer I (Fig. 24a) onto a $Si(111) - \sqrt{3} \times \sqrt{3}\, Ag$ surface through evaporation. All STM and STS measurements were performed at 5 K. Our *dI/dV* spectra were measured by lock-in technique with a modulation signal of 15 mV (rms) and 2000 Hz. Details for the preparation and separation of Dy@C82 isomer I were described elsewhere [81,82].

In Fig. 24, a set of STM images and *dI/dV* maps of a Dy@C_{82} molecule was given. The topography images show rich internal patterns, such as slightly curved bright stripes at the negative voltage (Fig. 24b) and some bright pentagon and hexagon rings at the positive voltage (Figs. 24c,d). In contrast to C_{60}, which has I_h symmetry and only one unique carbon site, the Dy@C_{82} isomer I is a metallofullerene in which the Dy atom lies along a C_2 axis on the six-membered ring of the C_{2v}-C_{82} cage [77]. So it has many nonequivalent sites due to its low symmetry, and we cannot deduce the orientation of

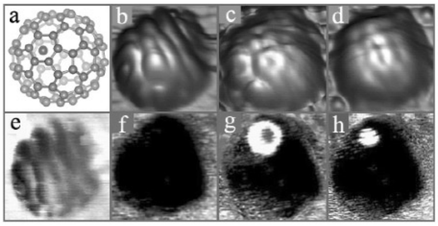

Fig. 24 (a) Structure model of a Dy@C_{82} isomer I molecule. (b–d) STM images of a Dy@C_{82} molecule taken at $V = -1.3$, 1.4, and 1.8 V. (e–h) *dI/dV* maps of the same Dy@C_{82} molecule taken at $V = -1.3$, 2.2, 2.0, and 2.1 V.

Dy@C_{82} with these STM images alone was done for C_{60} (see the sections “Native structure of C_{60} revealed by STM” and “Identifications of molecular orientations on surfaces”).

The *dI/dV* spatial maps of Dy@C_{82} at most V_S we measured show either a bright mesh structure (Fig. 24e) or a fully dark hollow (Fig. 24f). Only at certain positive-V_S (2.0 and 2.1 V), we observed a locally bright ring or dot (Figs. 24g,h). These *dI/dV* maps reveal detail in the electronic structure that cannot be observed in topographs [80]. We will show that the off-center bright spot in the hollow carbon cage is related to a metal-cage hybrid state. Our calculations were carried out using DFT with LDA implemented with the Dmol^3 package [73]. The Vosko–Wilk–Nusair local correlation functional [83] and all-electron calculations with scalar relativistic corrections were used.

Figure 25 shows the energy level diagram of a free Dy@C_{82} molecule. The orbital population analysis shows that the MOs of Dy@C_{82} can be divided into three types: cage-dominated [type I, Fig. 25-I], metal-dominated [type II, Fig. 25-II], and metal-cage hybrid [type III, Figs. 25-III and IV] orbitals. In the occupied valence-band region, only type I and II orbitals exist. In the unoccupied conduction-band region, however, there are two metal-cage hybrid orbitals at around 2 eV above the HOMO. In these orbitals, there is a strong hybridization between the Dy 6s orbital and the 2s and 2p orbitals of some specific C atoms. This kind of hybridization can result in a very local distribution of the LDOS on the fullerene cage. Since type I orbitals are irrelevant to the encapsulated metal atom, and type II orbitals are localized inside the fullerene cage that cannot be detected by the STS, mapping the metal-cage hybrid orbitals becomes the crux to detect the metal atom in the fullerene cage.

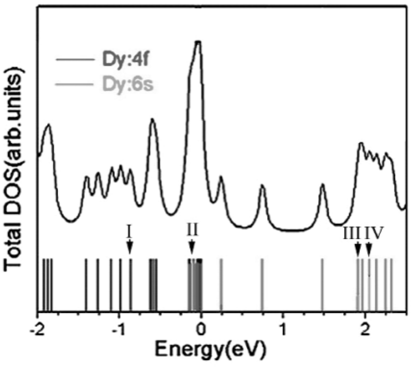

Fig. 25 The DOS and energy level structure of a free Dy@C_{82} molecule. The zero of energy is shifted to the HOMO. The lengths and colors of lines represent orbital populations from different atomic orbitals.

As an example, the spatial LDOS distribution of the second hybrid orbital at 2.05 eV (type IV, Fig. 25-IV) is presented in Fig. 26a (according to a standard molecular orientation, see Fig. 26b). The LDOS value at the two carbon atoms in the six-membered ring of the cage nearest to the Dy atom is much larger than that at other carbon atoms. One can expect that the *dI/dV* map of the hybrid orbital at 2.05 eV should be two or one bright dots, depending on the orientation of the molecule. This explains the observed off-center bright spot in the hollow carbon cage at around 2 V. Figures 26c–f show the simulated STM images and *dI/dV* maps by assuming the Dy@C_{82} molecule adsorbed on the surface with a certain orientation (Fig. 26g). The agreement between experiment (Figs. 24c,d,g,h) and theory is quite good. We notice that to understand all observed STM images and *dI/dV* maps, the molecule-substrate interaction and STM tip trajectory should be taken into account.

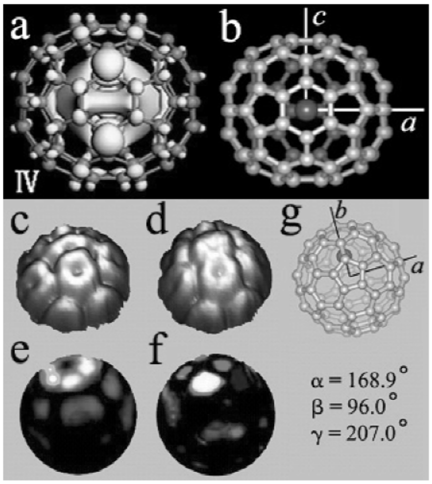

Fig. 26 (a) Isosurface of the electron density with isovalue of 5.0×10^{-4} e/Å^3 for the orbital at +2.05 eV. (b) A standard Dy@C_{82} molecular orientation in which the C_2 axis defines the z direction. (c–f) Simulated STM images for $V = -1.4$ and 1.8 V and simulated *dI/dV* maps at $E = 1.95$ and 2.05 eV, respectively. (g) Molecular orientation on the Ag surface. The three Euler angles are relative to the standard orientation of Dy@C_{82} defined in (b).

Our experimental observations of the metal-cage hybrid states support that the orbital hybridization and charge transfer constitute a complete picture for the interaction between the cage and metal atom [82,84]. Detecting the energy-resolved metal-cage hybrid states of a single endohedral metallofullerene provides not only the information for the metal-cage interaction, but also the geometrical and orientational information about the metallofullerene. This technique may find interesting applications in the fields of in situ characterization and diagnostics of metallofullerene-based nanodevices.

SINGLE-MOLECULAR MANIPULATION AND MOLECULAR ELECTRONICS

Scientists had a long dream to ultimately have the ability to fabricate or construct new materials and devices at the level of single atom or even single bond. In the last decade, scientists have demonstrated many examples of single-atom manipulation and single-molecular chemistry of bond cutting/forming with the help of STM [3,4]. These operations were realized by precisely controlling tip–sample interactions or by using the electric field between the tip and sample [4]. For example, by changing the tip bias, an “atomic switch” realized by repeated transfer of a Xe atom between the STM tip and a Ni(110) substrate was demonstrated by D. M. Eigler et al. [85]. T. Komeda et al. had investigated the mechanism of the chemical reaction of the benzene molecule adsorbed on the Cu(110) surface induced by the injection of tunneling electrons using STM. The dissociation of C–H bonds that occurred in a benzene molecule with the dosing of tunneling electrons from the STM tip induced a bonding geometry change from flat-lying to up-right configuration [86]. However, it is interesting and fundamentally important to look for novel molecular structures with the desired functions that may be applied in future devices. Here we will show two examples of the construction of novel molecular structures with unique electronic properties by the techniques of single-molecular manipulation and the chemistry of bond cutting.

C_{60} molecular negative differential resistance (NDR) device [9,19]

The concept of the NDR effect was first introduced by Esaki in 1958 [87], and the resonant tunneling diodes based on the NDR effect have been widely used in electronic devices since the middle of the 1970s [88]. This tunneling diode is characterized by the phenomenon of decreasing current with increasing voltage in the certain range of the *I–V* curves.

It has been shown experimentally [89,90] and theoretically [91,92] that atomic-scale NDR could arise in the tunneling structures with an STM tip and a localized surface site when the LDOS of both the tip and the surface site have adequately narrow features.

We have successfully demonstrated the NDR molecular device based on the geometry of DBTJ involving two C_{60} molecules which have high degenerate and large separated levels: one is adsorbed on the Pt-Ir tip of an STM and the other is physically adsorbed on the surface of the hexanethiol SAMs [19]. Such controllable tunneling structure and the associated known electronic states ensure the stability and reproducibility of the NDR device.

In the experiment, when the STM tip is brought close enough to a C_{60} island, a C_{60} molecule is preferentially adsorbed onto it [85]. This is because the fullerenes are weakly bound by van der Waals interaction to each other and to the SAM. Owing to the enhanced metal-C_{60} interactions, the attached C_{60} molecule can be stable at the apex of the tip. The attachment of a C_{60} molecule to the tip is a reversible process. When applying a voltage pulse of about 6 V, the adsorbed C_{60} on the tip will desorb. STS data was collected on C_{60} molecules after the adsorption of a C_{60} onto the tip as shown in Fig. 27, where (a) and (b) correspond to the tunneling structures of bare Pt-Ir tip on C_{60}, and C_{60} tip on C_{60}, respectively.

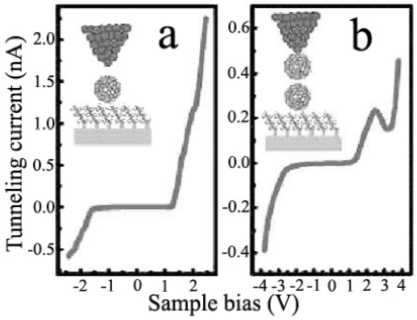

Fig. 27 The *I–V* curves obtained for two kinds of tunneling structures, as shown in the insets. (a) and (b) correspond to bare Pt-Ir tip and C_{60} tip on C_{60}/SAM, respectively.

It is interesting to note that when C_{60} molecules are separately adsorbed on the tip and on the thiols, an obvious NDR at the positive-V_S is observed in the *I–V* curve (Fig. 27b). This approves the assumption that the NDR phenomenon may be due to the narrow structure in the LDOS of the C_{60} molecules on both electrodes.

A theoretic simulation was performed to further confirm that the NDR indeed originated from the tunneling between two C_{60} molecules. In the simulation, the energy levels of a free C_{60} molecule were calculated by the discrete variational-LDA method [34,35]. Then, the LDOS of the C_{60} molecules on both electrodes were derived from the Lorentzian broadening of these discrete energy levels [93]. The Lorentzian width depends on the coupling with the environments, as well as on the temperature. The simulated *I–V* curve (lower part of Fig. 28a) reproduces the positive sample bias part of the measured STS with NDR (Fig. 27b). However, in the negative-bias range, the simulated result predicts NDR, which does not appear in the experimental result. Because of the interaction between C_{60} and Pt atoms through orbital mixing, the unoccupied states of the C_{60} adsorbed on the tip are more extended than the occupied states. It is expected that peaks in the unoccupied states are more broadening than that in the occupied states. This may be the reason for the absence of NDR in the negative-bias range (Fig. 28b).

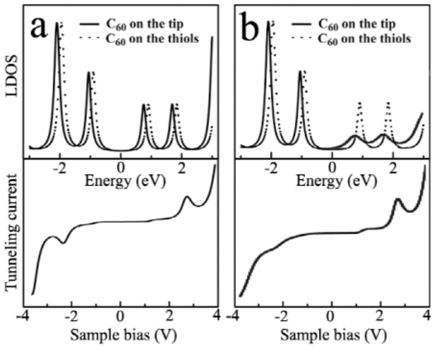

Fig. 28 The upper parts are the LDOS of C_{60} on the tip and C_{60} on the thiols involved in the simulations. (a) Identical and (b) different Lorentzian widths are assumed for the occupied and unoccupied states of the C_{60} on the tip. The lower parts are the corresponding calculated *I–V* curves.

Kondo effect in an artificial molecular structure [20]

The Kondo effect arises from the coupling between localized spins and conduction electrons, and at sufficiently low temperatures, it can lead to change in the transport properties through scattering or resonance effects [94]. We show here that the Kondo effect arising from magnetic ions on the surface of a nonmagnetic conductor can be controlled by changing their chemical environment. [20].

A submonolayer of CoPc molecules was adsorbed onto a Au(111) surface through thermal evaporation. STM images show protruding four-lobed structures with a bright spot at the center, which is consistent with the molecular structure (Fig. 29c2). When we apply a positive high-voltage (more than 3.3 V) pulse (Fig. 29a) over the edge of a lobe, the *I–t* curve (Fig. 29b) shows two sudden drops. We consider this a dehydrogenation process of the CoPc molecule [86]. The two drops in *I–t* curve indicate the sequential dissociation of the two H atoms from the benzene ring. Topographic image shows that the bright lobe disappeared after the voltage pulse (Fig. 29b inset). When all four lobes were cut to obtain the final dehydrogenated CoPc (d-CoPc) molecule (Figs. 29d1,d2), a marked increase of ~0.8 Å in apparent height at the center indicated either a strong conformational change of the molecular structure or a redistribution of the LDOS of the molecule. Moreover, the d-CoPc molecule on the Au(111) surface was difficult to move with the STM tip, indicating a strong interaction between the molecule and substrate.

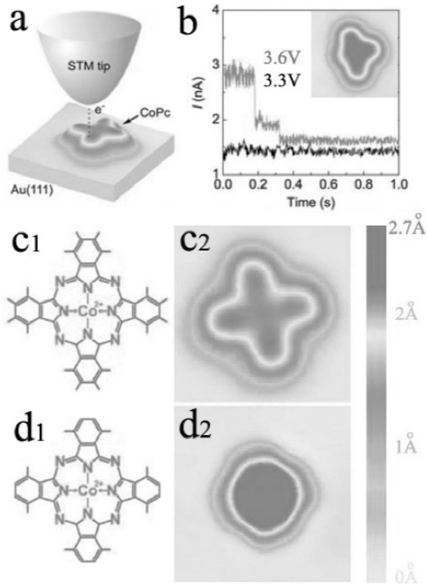

Fig. 29 STM tip-induced dehydrogenation of a single CoPc molecule. (a) Diagram of the dehydrogenation induced by the STM current. (b) Current vs. time during two different voltage pulses on the brink of one lobe. Black and gray lines correspond to 3.3 and 3.6 V, respectively. (b) Inset shows the result after one step of the dehydrogenation process. (c1,d1) Structural formula of a single CoPc molecule before and after four dehydrogenation processes. (c2,d2) STM images of an intact CoPc and a d-CoPc, respectively (25 × 25 Å). The color scale represents apparent heights, ranging from 0 (low) to 2.7 Å (high).

Typical differential conductance *dI*/*dV* spectra near the Fermi level (Fig. 30a) were measured precisely at the center of an intact CoPc and a d-CoPc molecule with the same tip. The *dI*/*dV* spectra were obtained using a lock-in amplifier [17,18]. For the intact CoPc molecule at 5 K, the well-characterized Co dz^2 orbital-mediated tunneling (OMT) peak [95–98] was observed centered around 150 meV below E_F. This peak disappears completely in the *dI*/*dV* spectrum of d-CoPc. Instead, a Kondo resonance peak arises immediately below E_F (–6 ± 3 meV), with an asymmetric shape and a narrow width of ~50 meV. After we elevated the temperature from 5 to 150 K, the resonance peak height for d-CoPc decreased by about a factor of 4 (Fig. 30a). Figures 30b and c show the good fit of the peak at different temperatures in the Fano model [99], which has been successfully applied to surface Kondo systems to describe the quantum interference between a localized magnetic impurity and a continuum [100,101].

According to the fittings we made (Figs. 30b,c), the Kondo temperature T_K of d-CoPc is estimated to be ~208 K, which is much higher than any previously reported temperature for magnetic atoms [100–102] or clusters [103] on surfaces.

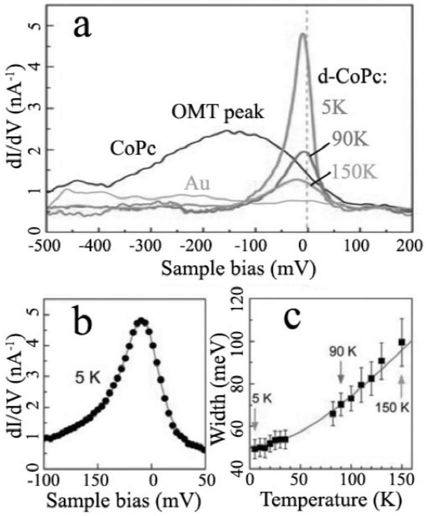

Fig. 30 (a) Typical *dI/dV* spectra measured at the centers of a CoPc molecule at 5 K (showing a dz^2 OMT peak) and a d-CoPc molecule at 5, 90, and 150 K. Spectra from bare Au(111) are shown for comparison. (b) A fit (line) to the resonance at 5 K in (a) according to the Fano model. Black symbols indicate experimental results. (c) The resonance width against measured temperature. Error bars represent standard deviations.

First-principles studies were carried out to understand the experimental observations. It is shown that the interaction between the planar CoPc (Figs. 31a,b) molecule and substrate clearly changes the electronic structure and magnetic property of the CoPc molecule. In the CoPc adsorption system, the magnet moment of the Co atom is completely quenched by the molecule-substrate interaction (Fig. 31c), while in a free CoPc molecule, the Co atom has unpaired d-electrons and the magnetic moment is 1.09 Bohr magnetons (μB).

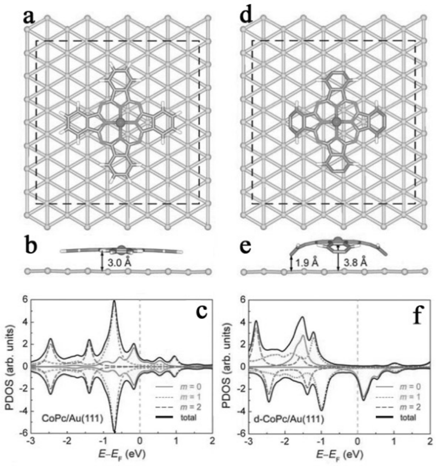

Fig. 31 (a,b,d,e) Top and side views of the optimized computational model for the CoPc/Au(111) and d-CoPc/Au(111) adsorption system. (c,f) The PDOS of the Co atom in a CoPc and a d-CoPc molecule on a Au(111) surface, respectively. The lines represent the total PDOS and its $m = 0$, $|m| = 1$, and $|m| = 2$ components, respectively.

Dehydrogenation induces a marked change of the molecular structure (Figs. 31d,e), so that the d-CoPc molecule on Au(111) is no longer planar. The central Co atom in the d-CoPc molecule shifts upward remarkably. More importantly, the magnetic moment is recovered for the d-CoPc adsorption system (Fig. 31f). The magnetic moment of the d-CoPc molecule is now 1.03 μB, very close to the value of a free CoPc molecule, and this induced the Kondo effect.

To understand the high Kondo temperature in the d-CoPc/Au(111) system, we compared its partial density of states (PDOS) with that of a single Co adatom on a Au(111) surface (Fig. 32) [104]. According to theoretical models for the Kondo temperature T_K [104,105], T_K increases monotonically as the on-site Coulomb repulsion U decreases or as the half-width Δ increases ($T_K = D_0 e^{-\pi U/8\Delta M}$, where D is a prefactor and M is the degeneracy number). The average spin splitting of the d-CoPc/Au(111) system is smaller than that of Co/Au(111), so the U of the d-CoPc/Au(111) system is smaller than that of the Co/Au(111) system. Moreover, the Δ of the hybridized d-level of the d-CoPc/Au(111) system is greater than that of the Co/Au(111) system. Previous experiments [101] reported that T_K for Co/Au(111) is ~75 K; thus, our experimental finding of a higher T_K for the d-CoPc on Au(111) is in qualitative agreement with theory.

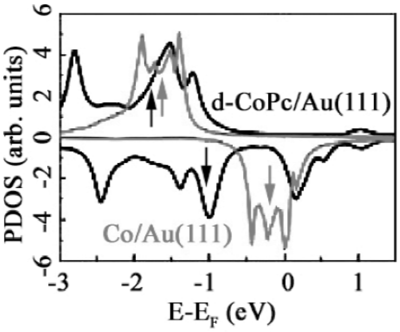

Fig. 32 Comparison of the total PDOS of an isolated Co atom on a hollow site of a Au(111) surface with that of a d-CoPc molecule on Au(111). Arrows indicate the energy positions of the spin-polarized PDOS centroids of the Co atom.

SUMMARY

We have reviewed our recent STM work on single molecules and their assemblies. The STM images of single molecules and their assemblies always show rich intramolecular fine structures or patterns. But the fine structures in STM images usually cannot be directly related to the molecular native structures owing to many intrinsic and extrinsic factors. The V_S, tip structures, substrate influence, and even the DOS distribution of the molecules all affect the imaging of single molecules or their assemblies. We have shown that only when the interaction of molecule and substrate is blocked is it possible to visualize intrinsic MOs directly by high-resolution STM images such as the system of C_{60}/thiol/Au. In most cases, the topography images of the molecules should be understood with the help of theoretical calculations and simulations, and thus we can understand not only the molecular structure but also the binding configurations and the orientations of the adsorbed molecules with respect to the substrate.

STM provides a unique technique for probing the LDOS on a subnanometer scale, but similar to the topography image there are still difficulties in the interpretation of the scanning tunneling spectrum of single molecules. We briefly discussed three different kinds of measurement configurations and their effects on the electronic measurements of a single molecule with an STM: the DOS of molecules may always be affected by being directly contacted to the two-electrode mode or SBTJ geometry. When we measure the *I–V* curve of a molecule in a DBTJ, the intrinsic electronic properties of the molecule will be obtained. Moreover, with the help of orthodox theory, the information of the gap between LUMO and HOMO as well as the discrete energy level structures of the molecules could be obtained from the SET spectrum.

For some molecular structures, the topography image and STS are still insufficient for fully understanding their bonding nature and electronic structure, a *dI/dV* mapping method that spatially maps the intensity of LDOS in a narrow energy window near $e \cdot V_S$ is helpful. As an example, we showed imaging of the MO and understanding the metal-cage interactions in a Dy@C_{82} molecule. The results of energy-dependent intramolecular patterns in *dI/dV* maps and theoretical calculations indicated that there is strong orbital hybridization between the Dy atom and the carbon cage.

Single-molecular manipulation and single-molecular bond-selective chemistry with the help of an STM tip is a unique and powerful technique for not only fabricating novel nanostructures with desired functions but also for helping us understand important physics and chemistry at the level of the single-molecular and even single bond. As examples, a molecular NDR device and an artificial nanostructure that shows clear Kondo effect were demonstrated by manipulating the C_{60} molecule and by applying dehydrogenation processes on a CoPc molecule, respectively.

ACKNOWLEDGMENTS

The National Natural Science Foundation of China, the Ministry of Science and Technology of China, the National Project for the Development of Key Fundamental Sciences in China, and the NKBRSF of China supported these works. Special thanks goes to Prof. J. L. Yang and his coworkers, who did all the computational chemistry calculations reported here.

REFERENCES

1. G. Binnig, H. Rohrer, Ch. Gerber, E. Weibel. *Phys. Rev. Lett.* **49**, 57 (1982).
2. C. J. Chen. *Introduction to Scanning Tunneling Microscopy*, Oxford University Press, Oxford (1993).
3. W. Ho. *J. Chem. Phys.* **117**, 11033 (2002).
4. S. W. Hla. *J. Vac. Sci. Technol. B* **23**, 1351 (2005).
5. T. W. Odom, J. L. Huang, P. Kim, C. M. Lieber. *Nature* **391**, 62 (1998).
6. H. Neddermeyer. *Rep. Prog. Phys.* **59**, 701 (1996).
7. T. A. Jung, R. R. Schlittler, J. K. Gimzewski. *Nature* **386**, 696 (1997).
8. B. C. Stipe, M. A. Rezaei, W. Ho. *Science* **280**, 1732 (1998).
9. C. G. Zeng, J. G. Hou. *Mesoscopic Tunneling Devices*, N. Hiroshi (Ed.), p. 203, Research Signpost, Kerala (2004).
10. J. Zhao B. Miao, L. Zhao, J. G. Hou. *Int. J. Nanotechnol.* **1**, 157 (2004).
11. B. Li, H. Q. Wang, J. L. Yang, J. G. Hou. *Ultramicroscopy* **98**, 317 (2004).
12. F. Besenbacher. *Rep. Prog. Phys.* **59**, 1737 (1996).
13. K. D. Wang, C. Zhang, M. M. T. Loy, X. D. Xiao. *Phys. Rev. Lett.* **94**, 036103 (2005).
14. J. G. Hou, J. L. Yang, H. Q. Wang, Q. X. Li, C. G. Zeng, L. F. Yuan, B. Wang, D. M. Chen, Q. S. Zhu. *Nature* **409**, 304 (2001).
15. J. G. Hou, J. L. Yang, H. Q. Wang, Q. X. Li, C. G. Zeng, H. Lin, B. Wang, D. M. Chen, Q. S. Zhu. *Phys. Rev. Lett.* **83**, 3001 (1999).
16. H. Q. Wang, C. G. Zeng, Q. X. Li, B. Wang, J. L. Yang, J. G. Hou, Q. S. Zhu. *Surf. Sci.* **442**, L1024 (1999).
17. K. D. Wang, J. Zhao, S. F. Yang, L. Chen, Q. X. Li, B. Wang, S. H. Yang, J. L. Yang, J. G. Hou, Q. S. Zhu. *Phys. Rev. Lett.* **91**, 185504 (2003).
18. J. Zhao, C. G. Zeng, X. Chen, K. D. Wang, G. W. Wang, J. L. Yang, J. G. Hou, Q. S. Zhu. *Phys. Rev. Lett.* **95**, 045502 (2005).
19. C. G. Zeng, H. Q. Wang, B. Wang, J. L. Yang, J. G. Hou. *Appl. Phys. Lett.* **77**, 3595 (2000).

20. A. D. Zhao, Q. X. Li, L. Chen, H. J. Xiang, W. H. Wang, S. Pan, B. Wang, X. D. Xiao, J. L. Yang, J. G. Hou, Q. S. Zhu. *Science* **309**, 1542 (2005).
21. L. F. Yuan, J. L. Yang, H. Q. Wang, C. G. Zeng, Q. X. Li, B. Wang, J. G. Hou, Q. S. Zhu, D. M. Chen. *J. Am. Chem. Soc.* **125**, 169 (2003).
22. C. G. Zeng, B. Li, B. Wang, H. Q. Wang, K. D. Wang, J. L. Yang, J. G. Hou, Q. S. Zhu. *J. Chem. Phys.* **117**, 851 (2002).
23. B. Li, C. G. Zeng, Q. X. Li, B. Wang, L. F. Yuan, H. Q. Wang, J. L. Yang, J. G. Hou, Q. S. Zhu. *J. Phys. Chem. B* **107**, 972 (2003).
24. P. Hohenberg, W. Kohn. *Phys. Rev. B* **136**, 864 (1964).
25. W. Kohn, L. J. Sham. *Phys. Rev. A* **140**, 1133 (1965).
26. C. J. Chen. *Phys. Rev. Lett.* **69**, 1656 (1992).
27. T. Hashizume, K. Motai, X. D. Wang, H. Shinohara, Y. Maruyama, K. Ohno, Y. Nishina, H. W. Piclering, Y. Kuk, T. Sakurai. *Phys. Rev. Lett.* **71**, 2959 (1993).
28. H. R. Kroto, J. R. Heath, S. C. O'Brien, R. F. Curl, R. E. Smalley. *Nature* **318**, 162 (1985).
29. W. Krätschmer, L. D. Lamb, K. Fostiropoulos, D. R. Huffman. *Nature* **347**, 354 (1990).
30. T. Hashizume, X. D. Wang, Y. Nishina, H. Shinohara, Y. Saito, Y. Kuk, T. Sakurai. *Jpn. J. Appl. Phys.* **31**, L880 (1993).
31. X. D. Wang, T. Hashizume, H. Shinohara, Y. Sato, Y. Nishina, T. Sakurai. *Jpn. J. Appl. Phys.* **31**, L983 (1992).
32. R. Gaisch, R. Berndt, J. K. Gimzewski, B. Reihl, R. R. Schlittler, W. D. Schneider, M. Tschudy. *J. Vac. Sci. Technol. B* **12**, 2153 (1994).
33. P. Moriarty, Y. R. Ma, M. D. Upward, P. H. Beton. *Surf. Sci.* **407**, 27 (1998).
34. B. Delley, D. E. Ellis. *J. Chem. Phys.* **76**, 1949 (1982).
35. B. Delley, D. E. Ellis, A. J. Freeman, E. J. Baerends, D. Post. *Phys. Rev. B* **27**, 2132 (1983).
36. S. K. Sinha. *Ordering in Two Dimensions*, North-Holland, Amsterdam (1980).
37. J. Tersoff, D. R. Hamann. *Phys. Rev. B* **31**, 805 (1985).
38. A. M. Rao, P. Zhou, K. A. Wang, G. T. Hager, J. M. Holden, Y. Wang, W. T. Lee, X. X. Bi, P. C. Eklund, D. S. Cornett, M. A. Duncan, I. J. Amster. *Science* **259**, 955 (1993).
39. M. Ata, N. Takahashi, K. Nojima. *J. Phys. Chem.* **98**, 9960 (1994).
40. N. Takahashi, H. Dock, N. Matsuzawa, M. Ata. *J. Appl. Phys.* **74**, 5790 (1993).
41. Y. Nakamura, Y. Mera, K. Maeda. *Appl. Phys. Lett.* **77**, 2834 (2000).
42. K. Allen, F. Hellman. *Phys. Rev. B* **60**, 11765 (1999).
43. M. Menon, K. R. Subbaswamy, M. Sawtarie. *Phys. Rev. B* **49**, 13966 (1994).
44. G. B. Adams, J. B. Page, O. F. Sankey, M. O'Keeffe. *Phys. Rev. B* **50**, 17471 (1994).
45. G. W. Wang, K. Komatsu, Y. Murata, M. Shiro. *Nature* **387**, 583 (1997).
46. S. Yoshimoto, R. Narita, E. Tsutsumi, M. Matsumoto, K. Itaya, O. Ito. *Langmuir* **18**, 8518 (2002).
47. M. Matsumoto, J. Inukai, E. Tsutsumi, S. Yoshimoto, K. Itaya, O. Ito, K. Fujiwara, M. Murata, Y. Murata, K. Komatsu. *Langmuir* **20**, 1245 (2004).
48. A. Ulman. *Chem. Rev.* **96**, 1533 (1996).
49. F. Schreiber. *Prog. Surf. Sci.* **65**, 151 (2000).
50. A. Ulman. *Thin Films: Self-Assembled Monolayers of Thiols*, Academic Press, San Diego, CA (1998).
51. G. E. Poirier, E. D. Pylant. *Science* **272**, 1145 (1996).
52. C. A. Widrig, C. A. Alves, M. D. Porter. *J. Am. Chem. Soc.* **113**, 2805 (1991).
53. E. Delamarche, B. Michel, H. A. Biebuyck, C. Gerber. *Adv. Mater.* **8,** 719 (1996).
54. G. E. Poirier, M. J. Tarlov, H. E. Rushmeir. *Langmuir* **10**, 3383 (1994).
55. J. P. Bucher, L. Santesson, K. Kern. *Appl. Phys. A* **59**, 135 (1994).
56. F. T. Arce, M. E. Vela, R. C. Salvarezza, A. J. Arvia. *J. Chem. Phys.* **109**, 5703 (1998).
57. M. Kawasaki, T. Sato, T. Tanaka, K. Takao. *Langmuir* **16**, 1719 (2000).
58. H. Sellers, A. Ulman, Y. Shnidman, J. E. Eilers. *J. Am. Chem. Soc.* **115**, 9389 (1993).

59. T. W. Li, I. Chao, Y. T. Tao. *J. Phys. Chem.* **102**, 2935 (1998).
60. L. H. Dubois, R. G. Nuzzo. *Annu. Rev. Phys. Chem.* **43**, 437 (1992).
61. H. Park, A. K. L. Lim, J. Park, A. P. Alivisatos, P. L. McEuen. *Appl. Phys. Lett.* **75**, 301 (1999).
62. H. Park, J. Park, A. K. L. Lim, E. H. Anderson, A. P. Alivisatos, P. L. McEuen. *Nature* **407**, 57 (2000).
63. R. C. Haddon, L. E. Brus, K. Raghavachari. *Chem. Phys. Lett.* **125**, 459 (1986).
64. S. Saito, A. Oshima. *Phys. Rev. Lett.* **66**, 2637 (1991).
65. X. Yao, T. G. Ruskell, R. K. Workman, D. Sarid, D. Chen. *Surf. Sci.* **366**, L743 (1996).
66. J. Taylor, H. Guo, J. Wang. *Phys. Rev. B* **63**, 121104 (2001).
67. M. Amman, R. Wilkins, E. Ben-Jacob, P. Maker, R. Jaklevic. *Phys. Rev. B* **43**, 1146 (1991).
68. A. E. Hanna, M. Tinkham. *Phys. Rev. B* **44**, 5919 (1991).
69. N. Camillone, T. Y. B. Leung, P. Schwartz, P. Eisenberger, G. Scoles. *Langmuir* **12**, 2737 (1996).
70. M. D. Porter, T. B. Bright, D. L. Allara, C. E. D. Chidsey. *J. Am. Chem. Soc.* **109**, 3559 (1987).
71. B. Wang, K. D. Wang, W. Lu, J. L. Yang, J. G. Hou. *Phys. Rev. B* **63**, 35403 (2001).
72. U. Reuther, A. Hirsch. *Carbon* **38**, 1539 (2000).
73. Dmol^3 is a DFT-based package with atomic basis distributed by Accelrys. [B. Delley. *J. Chem. Phys.* **92**, 508 (1990)].
74. H. Shinohara. *Rep. Prog. Phys.* **63**, 843 (2000).
75. C. H. Park, B. O. Wells, J. DiCarlo, Z. X. Shen, J. R. Salem, D. S. Bethune, C. S. Yannoni, R. D. Johnson, M. S. de Vries, C. H. Booth, F. Bridges, P. Pianetta. *Chem. Phys. Lett.* **213**, 196 (1993).
76. E. Nishibori, M. Takata, M. Sakata, M. Inakuma, H. Shinohara. *Chem. Phys. Lett.* **298**, 79 (1998).
77. S. Iida, Y. Kubozono, Y. Slovokhotov, Y. Takabayashi, T. Kanbara, T. Fukunaga, S. Fujiki, S. Emura, S. Kashino. *Chem. Phys. Lett.* **338**, 21 (2001).
78. Y. Kubozono, Y. Takabayashi, K. Shibata, T. Kanbara, S. Fujiki, S. Kashino, A. Fujiwara, S. Emura. *Phys. Rev. B* **67**, 115410 (2003).
79. S. Hino, K. Umishita, K. Iwasaki, T. Miyazaki, T. Miyake, K. Kikuchi, Y. Achiba. *Chem. Phys. Lett.* **281**, 115 (1997).
80. X. Lu, M. Grobis, K. H. Khoo, S. G. Louie, M. F. Crommie. *Phys. Rev. Lett.* **90**, 096802 (2003).
81. H. Huang, S. H. Yang. *Chem. Mater.* **12**, 2715 (2000).
82. H. Huang, S. H. Yang, X. Zhang. *J. Phys. Chem. B* **104**, 1473 (2000).
83. S. H. Vosko, L. Wilk, M. Nusair. *Can. J. Phys.* **58**, 1200 (1980).
84. B. Kessler, A. Bringer, S. Cramm, C. Schlebusch, W. Eberhardt, S. Suzuki, Y. Achiba, F. Esch, M. Barnaba, D. Cocco. *Phys. Rev. Lett.* **79**, 2289 (1997).
85. D. M. Eigler, C. P. Lutz, W. E. Rudge. *Nature* **352**, 600 (1991).
86. T. Komeda, Y. Kim, Y. Fujita, Y. Sainoo, M. Kawai. *J. Chem. Phys.* **120**, 15 (2004).
87. L. Esaki. *Phys. Rev.* **109**, 603 (1958).
88. M. C. Roco, R. S. Williams, P. Alivisatos. *Nanotechnology Research Directions: IWGN Workshop Report,* NSTC/CT/IWGN (1999).
89. I. W. Lyo, P. Avouris. *Science* **245**, 1369 (1989).
90. P. Bedrossian, D. M. Chen, K. Mortensen, J. A. Golovchenko. *Nature* **342**, 258 (1989).
91. Y. Xue, S. Datta, S. Hong, R. Reifenberger, J. I. Henderson, C. P. Kubiak. *Phys. Rev. B* **59**, R7852 (1999).
92. N. D. Lang. *Phys. Rev. B* **55**, 9364 (1997).
93. N. D. Lang, A. R. Williams. *Phys. Rev. B* **18**, 616 (1978).
94. A. C. Hewson. *The Kondo Problem to Heavy Fermions*, Cambridge University Press, Cambridge (1993).
95. P. A. Reynolds, B. N. Figgis. *Inorg. Chem.* **30**, 2294 (1991).
96. X. Lu, K. W. Hipps, X. D. Wang, U. Mazur. *J. Am. Chem. Soc.* **118**, 7197 (1996).
97. J. M. Assour. *J. Am. Chem. Soc.* **87**, 4701 (1965).
98. D. E. Barlow, L. Scudiero, K. W. Hipps. *Langmuir* **20**, 4413 (2004).

99. U. Fano. *Phys. Rev.* **124**, 1866 (1961).
100. J. Li, W. D. Schneider, R. Berndt, B. Delley. *Phys. Rev. Lett.* **80**, 2893 (1998).
101. V. Madhavan, W. Chen, T. Jamneala, M. F. Crommie, N. S. Wingreen. *Science* **280**, 567 (1998).
102. T. Jamneala, V. Madhavan, W. Chen, M. F. Crommie. *Phys. Rev. B* **61**, 9990 (2000).
103. T. W. Odom, J. L. Huang, C. L. Cheung, C. M. Lieber. *Science* **290**, 1549 (2000).
104. O. Újsághy, J. Kroha, L. Szunyogh, A. Zawadowski. *Phys. Rev. Lett.* **85**, 2557 (2000).
105. H. Q. Lin, J. E. Hirsch. *Phys. Rev. B* **37**, 1864 (1988).